

The kaobook class

**Use this document as a template**

# **My PhD Thesis**

**Customise this page according to your needs**

Tobias Hangleiter\*

May 2, 2025

\* A  $\text{\LaTeX}$  lover/hater

The kaobook class

### **Disclaimer**

You can edit this page to suit your needs. For instance, here we have a no copyright statement, a colophon and some other information. This page is based on the corresponding page of Ken Arroyo Ohori's thesis, with minimal changes.

### **No copyright**

©© This book is released into the public domain using the CC0 code. To the extent possible under law, I waive all copyright and related or neighbouring rights to this work.

To view a copy of the CC0 code, visit:

<http://creativecommons.org/publicdomain/zero/1.0/>

### **Colophon**

This document was typeset with the help of KOMA-Script and L<sup>A</sup>T<sub>E</sub>X using the kaobook class.

The source code of this book is available at:

<https://github.com/fmarotta/kaobook>

(You are welcome to contribute!)

### **Publisher**

First printed in May 2019 by

The harmony of the world is made manifest in Form and Number, and the heart and soul and all the poetry of Natural Philosophy are embodied in the concept of mathematical beauty.

– D'Arcy Wentworth Thompson



# Contents

<b>Contents</b>	<b>v</b>
<b>I A FLEXIBLE PYTHON TOOL FOR FOURIER-TRANSFORM NOISE SPECTROSCOPY</b>	<b>1</b>
1 Introduction	3
2 Theory of spectral noise estimation	5
2.1 Spectrum estimation from time series . . . . .	6
2.2 Window functions . . . . .	8
2.3 Welch's method . . . . .	9
2.4 Parameters & Properties of the PSD . . . . .	10
3 The <code>python_spectrometer</code> software package	13
3.1 Package design and implementation . . . . .	13
3.1.1 Data acquisition . . . . .	13
3.1.2 Data processing . . . . .	15
3.2 Feature overview . . . . .	16
3.2.1 Serial spectrum acquisition . . . . .	17
3.2.2 Live spectrum acquisition . . . . .	20
4 Conclusion and outlook	23
<b>II CHARACTERIZATION AND IMPROVEMENTS OF A MILLIKELVIN CONFOCAL MICROSCOPE</b>	<b>27</b>
5 Introduction	29
6 Characterization of electrical performance	31
6.1 Electron temperature . . . . .	31
7 Characterization and improvements of the optical path	33
8 Vibration performance	35
8.1 Accelerometric vibration spectroscopy . . . . .	35
8.2 Optical vibration spectroscopy . . . . .	36
9 Conclusion & outlook	39
<b>III OPTICAL MEASUREMENTS OF ELECTROSTATIC EXCITON TRAPS IN SEMICONDUCTOR MEMBRANES</b>	<b>41</b>
<b>IV A FILTER-FUNCTION FORMALISM FOR UNITAL QUANTUM OPERATIONS</b>	<b>43</b>
10 Introduction	47
11 Filter function formalism for unital quantum operations	51
11.1 Transfer matrix representation of quantum operations . . . . .	51
11.1.1 Brief review of quantum operations and superoperators . . . . .	51
11.1.2 Liouville representation of the error channel . . . . .	52

11.2	Calculating the decay amplitudes . . . . .	57
11.2.1	Control matrix of a gate sequence . . . . .	58
11.2.2	Control matrix of a single gate . . . . .	60
11.3	Calculating the frequency shifts . . . . .	61
11.4	Computing derived quantities . . . . .	63
11.4.1	Average gate and entanglement fidelity . . . . .	63
11.4.2	State fidelity and measurements . . . . .	64
11.4.3	Leakage . . . . .	64
11.5	Performance analysis and efficiency improvements . . . . .	65
11.6	Periodic Hamiltonians . . . . .	65
11.7	Extending Hilbert spaces . . . . .	66
11.8	Operator bases . . . . .	67
11.9	Computational complexity . . . . .	68
<b>12</b>	<b>Software implementation</b>	<b>73</b>
12.1	Package overview . . . . .	73
12.2	Workflow . . . . .	74
<b>13</b>	<b>Example applications</b>	<b>77</b>
13.1	Singlet-triplet two-qubit gates . . . . .	77
13.2	Rabi driving . . . . .	79
13.3	Randomized Benchmarking . . . . .	81
13.4	Quantum Fourier transform . . . . .	84
<b>14</b>	<b>Further considerations</b>	<b>87</b>
<b>15</b>	<b>Conclusion and outlook</b>	<b>89</b>
<b>16</b>	<b>Monte Carlo and Lindblad master equation simulations</b>	<b>91</b>
16.1	Validation of QFT fidelities . . . . .	91
<b>17</b>	<b>Reconstruction by frequency-comb time-domain simulation</b>	<b>93</b>
<b>APPENDIX</b>		<b>95</b>
<b>A</b>	<b>Filter Functions</b>	<b>97</b>
A.1	Additional derivations . . . . .	97
A.1.1	Derivation of the single-qubit cumulant function in the Liouville representation . . . . .	97
A.1.2	Evaluation of the integrals in Equation 11.39 . . . . .	98
A.1.3	Simplifying the calculation of the entanglement infidelity . . . . .	98
A.2	Singlet-Triplet Gate Fidelity . . . . .	99
A.3	GRAPE-optimized gate set for QFT . . . . .	101
A.4	Convergence Bounds . . . . .	102
A.4.1	Magnus Expansion . . . . .	102
A.4.2	Infidelity . . . . .	103
A.5	Second-order concatenation . . . . .	104
<b>Bibliography</b>		<b>105</b>
<b>List of Terms</b>		<b>107</b>

# List of Figures

2.1	Generated by <code>img/tikz/spectrometer/lockin_dut.tex</code> . . . . .	5
2.2	Generated by <code>img/code/spectrometer/lorentz.py</code> . . . . .	7
2.3	Generated by <code>img/code/spectrometer/pyspeck.py</code> . . . . .	9
2.4	Generated by <code>img/code/spectrometer/pyspeck.py</code> . . . . .	9
2.5	Generated by <code>img/code/spectrometer/pyspeck.py</code> . . . . .	10
2.6	Generated by <code>img/tikz/spectrometer/daq_settings.tex</code> . . . . .	11
3.1	Generated by <code>img/tikz/spectrometer/speck_tree.tex</code> . . . . .	13
3.2	Generated by <code>img/code/spectrometer/pyspeck_workflow.py</code> . . . . .	17
3.3	Generated by <code>img/code/spectrometer/pyspeck_workflow.py</code> . . . . .	18
3.4	Generated by <code>img/code/spectrometer/pyspeck_workflow.py</code> . . . . .	19
3.5	Generated by <code>img/code/spectrometer/pyspeck_workflow.py</code> . . . . .	19
3.6	Generated by <code>img/code/spectrometer/pyspeck_workflow.py</code> . . . . .	19
3.7	Generated by <code>img/code/spectrometer/pyspeck_workflow.py</code> . . . . .	20
3.8	Generated by <code>img/code/spectrometer/pyspeck_live_view.py</code> . . . . .	21
6.1	Generated by <code>img/py/setup/transport.py</code> . . . . .	32
6.2	Generated by <code>img/py/setup/transport.py</code> . . . . .	32
6.3	Generated by <code>img/py/setup/transport.py</code> . . . . .	32
8.1	Generated by <code>img/py/setup/vibrations.py</code> . . . . .	36
8.2	Generated by <code>img/py/setup/vibrations.py</code> . . . . .	36
8.3	Generated by <code>img/py/setup/vibrations.py</code> . . . . .	36
8.4	Generated by <code>img/py/setup/vibrations.py</code> . . . . .	36
8.5	Generated by <code>img/py/setup/vibrations.py</code> . . . . .	37
11.1	Illustration of gate sequence . . . . .	59
11.2	Performance of the formalism using Equation 11.35 compared to a Monte Carlo method for a single gate as a function of problem dimension $d$ . Parameters are: $n_{\Delta t} = 1, n_{\alpha} = 3, n_{MC} = 100, f_{UV} = 10^2/\Delta t, n_{\omega} = 500$ where $n_{\alpha}$ is the number of noise operators considered, $n_{MC}$ the number of Monte Carlo trajectories over which is averaged, and $n_{\omega}$ the number of frequency samples. The calculation using filter functions clearly outperforms MC for small system sizes. For dimensions larger than $d \approx 100$ (roughly equivalent to 7 qubits) Monte Carlo (blue squares) performs better than the filter function (FF) calculation with transfer matrices (green triangles) for this set of parameters and processor due to the better scaling behavior. Using conjugation by unitaries (orange diamonds) significantly outperforms Monte Carlo (MC) also for large dimensions. While the fits to $t = ad^b$ (lines) underestimate the leading order exponent due to the data not being in the asymptotic regime, they support the expected relationship of complexity between the approaches. The inset shows the same data on a linear scale, highlighting the different scaling behaviors for large $d$ . . . . .	70
13.1	(a) Exchange interaction $J(\epsilon_{ij})$ for the CNOT gate presented in Reference <b>Cerfontaine2020b</b> as function of time. (b) Filter functions $F_{\epsilon_{ij}}$ for noise in the detunings evaluated on the computational subspace. The filter functions are modulated by oscillations at high frequencies due to numerical artifacts of the finite step size for the time evolution. The inset shows the filter functions in the DC regime on a linear scale with distinct peaks around $\omega = 2\pi/\tau$ and $\omega = 50/\tau$ ( $\tau = 50$ ns). (c)–(e) Computational subspace block of the first order approximation of the error transfer matrix, given by the cumulant function $\mathcal{K}_{\alpha\alpha}$ excluding second order contributions, for the CNOT gate and the three detunings $\alpha \in \{\epsilon_{12}, \epsilon_{23}, \epsilon_{34}\}$ . Note that in panel (e) the order of the rows and columns was permuted for better comparability. . . . .	79

13.2	Filter functions for weak (a) and strong (b) Rabi driving (20 identity gates in total). Grey dashed (dotted) lines indicate the respective drive (Rabi) frequencies $\omega_0$ ( $\Omega_R$ ). (a) Weak driving with $A/\omega_0 \ll 1$ . The filter function $F_{xx}$ for noise operator $\sigma_x$ is approximately constant up to the resonance frequency where it peaks sharply and then aligns with the filter function $F_{zz}$ for $\sigma_z$ . $F_{zz}$ peaks at the Rabi frequency before rolling off with $\omega^{-2}$ and a DC level that is almost ten orders of magnitude larger than the DC level of the transverse filter function $F_{xx}$ . (b) Strong driving with $A/\omega_0 \sim 1$ . Again $F_{zz}$ peaks at $\Omega_R$ whereas $F_{xx}$ has three distinct peaks at $\omega_0$ and $\omega_0 \pm \Omega_R$ . These features also appear at slightly higher frequencies in $F_{zz}$ due to the strong coupling. . . . .	81
13.3	Simulation of a standard randomized benchmarking (SRB) experiment using 100 random sequences per point for different gate and noise types (see the main text for an explanation of the gate type monikers). Dashed lines are fits of Equation 13.3 to the data while the solid black lines correspond to a zeroth-order SRB model with $A = B = 0.5$ and the true average gate infidelity per Clifford $r$ . Errorbars show the standard deviation of the SRB sequence fidelities, illustrating that for the “single” gate set noise correlations can lead to amplified destructive and constructive interference of errors. The same noise spectrum is used for all three error channels ( $\sigma_x, \sigma_y, \sigma_z$ ) and the large plots show the sum of all contributions. (a) Uncorrelated white noise with the noise power adjusted for each gate type so that the average error per gate $r$ is constant over all gate types. No notable deviation is seen between different gate types. (b) Correlated $1/f$ -like noise with noise power adjusted to match the average Clifford fidelity in (a). The decay of the “single” gateset differs considerably from that of the other gate sets and the SRB decay expected for the given average gate fidelity, whereas “naive” and “optimized” gates match the zeroth order SRB model well, indicating that correlations in the noise affect the relation between SRB decay and average gate fidelity in a gateset-dependent way. Inset: contributions from $\sigma_z$ -noise show that the sequence fidelity can be better than expected for certain gate types and noise channels. . . . .	84
13.4	quantum Fourier transform (QFT) circuit and filter function . . . . .	86
A.1	Filter functions of the voltage detunings $\epsilon_{ij}$ excluding (a) and including (b) the zero-padded identity matrix basis element $C_0^c \propto \text{diag}(1, 1, 1, 1, 0, 0)$ for the computational subspace. Evidently, including $C_0^c$ removes the DCG character, namely that $F_{\epsilon_{ij}}(\omega) \rightarrow 0$ as $\omega \rightarrow 0$ , of the gates but has little effect on the high-frequency behavior. As the pulse optimization minimizes, among other figures of merit, the infidelity of the final propagator mapped to the closest unitary on the computational subspace due to quasistatic and fast white noise, this indicates that excluding $C_0^c$ from the filter function corresponds to partially neglecting non-unitary components of the propagator on the computational subspace. . . . .	101
A.2	Control fields (top row) and corresponding filter functions (bottom row) of the GRAPE-optimized pulses in G. (a),(b) $X_0(\pi/2)$ ; (c),(d) $Y_0(\pi/2)$ ; (e),(f) $CR_{01}(\pi/2^3)$ . Note that the optimization is neither very sophisticated nor realistic as the algorithm only maximizes the systematic (coherent) fidelity $\text{tr}(UQ_{\text{targ}}^\dagger)/d$ and the randomly distributed initial control amplitudes are not subject to any constraints. . . . .	102







**Part I**

**A FLEXIBLE PYTHON TOOL FOR  
FOURIER-TRANSFORM NOISE  
SPECTROSCOPY**





## **Part II**

# **CHARACTERIZATION AND IMPROVEMENTS OF A MILLIKELVIN CONFOCAL MICROSCOPE**



# Introduction

5







# Characterization of electrical performance

6



## 6.1 Electron temperature

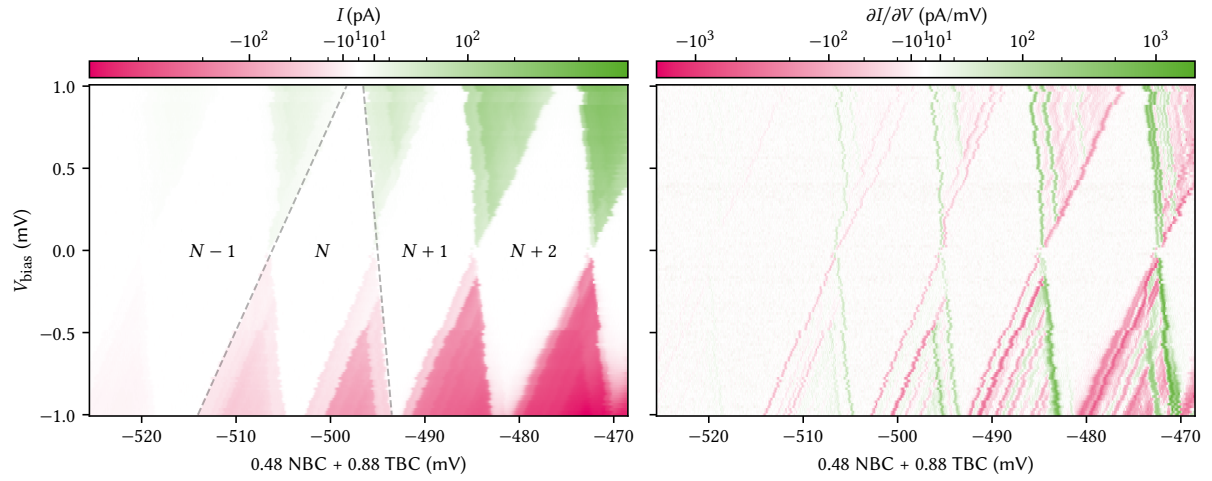


Figure 6.1

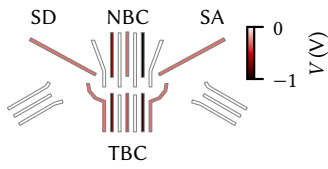


Figure 6.2

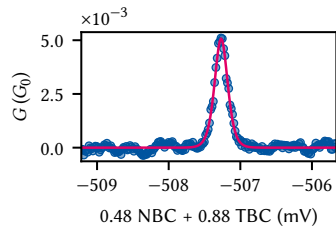


Figure 6.3

# Characterization and improvements of the optical path

7





# Vibration performance

A microscope's performance is limited chiefly by two factors; first and foremost the resolution and imaging fidelity are limited by the systematic aberrations introduced by the optics.<sup>1</sup> Various types of aberrations exist, and modern microscopes usually include a complex assembly of optics to compensate for these errors. The second factor is vibration noise. This becomes more significant the higher the resolution of the microscope simply because ambient, environmental vibrations within the range of human civilization is typically on the order of 100  $\mu\text{m/s}$  RMS [1]. Comparing that to transmission electron microscopes (TEMs) with atomic resolution, it is clear that these instruments require purpose-built rooms to reduce the vibration level to acceptable levels.

The demands on the microscope discussed in the present thesis are fortunately much more relaxed as the features we need to resolve are micron-sized. However, we face the additional challenge of ultra-low temperatures, or rather the manner in which they are achieved. The microscope is integrated into a *dry* dilution refrigerator (DR). In contrast to a *wet* DR, which uses a liquid Helium bath, these systems achieve the pre-cooling necessary for the  $^3\text{He}/^4\text{He}$  dilution refrigeration cycle to work by adding a secondary refrigeration mechanism, a pulse tube refrigerator (PTR). These are closed-cycle systems that work with  $^4\text{He}$  compressed to  $\sim 21$  bar on the high-pressure and  $\sim 7$  bar on the low-pressure side. A rotating valve connecting high and low pressure lines to the cryostat in turn produces alternating gas flow inside a regenerator, where the gas absorbs heat at the low-temperature end and deposits heat at the high-temperature end [2, 3]. In commercial PTRs the frequency of the pulses of Helium gas, determined by the rotary valve motor, is usually fixed at values around 1.5 Hz.

Naturally, the compressor, the rotary valve motor, and the Helium pulses themselves introduce vibrations into the cryostat. While the cold finger of the PTR is not rigidly connected to the cryostat interior,<sup>2</sup> the entire cold head assembly rests with rubber feet on the cryostat top plate in the system's delivery status. Thus, our microscope does not only encounter passive environmental vibrations but also the active disturbance from the PTR. To characterize and improve upon the vibration isolation, I performed vibration noise spectroscopy using the techniques and tools presented in Part I.<sup>3</sup> I employed two different approaches that I lay out in the following; first, using a commercial piezoelectric accelerometer (Section 8.1) and second, using the optical response of a spatial reflectance gradient (Section 8.2). As will become clear, the two approaches complement each other because they are sensitive to slightly different quantities.

## 8.1 Accelerometric vibration spectroscopy

Triggered by a sudden increase in visually observed vibrations in the microscope image, I performed vibration noise spectroscopy with a piezoelectric accelerometer. The main source of noise The DR was designed

1: Besides the limit set by the wavelength-dependent diffraction, of course.

2: In the Oxford Instruments Triton 450 copper braids connect the cold head to the first pulse tube stage (PT1) and second pulse tube stage (PT2) plates. There exist commercial systems that use gas exchange instead, see for example the CryoConcept HEXA-DRY series.

3: The endeavour was triggered by a sudden increase in visually observed vibrations in the microscope image. As it turned out, the cause was a damaged nanopositioner bearing rather than environmental.

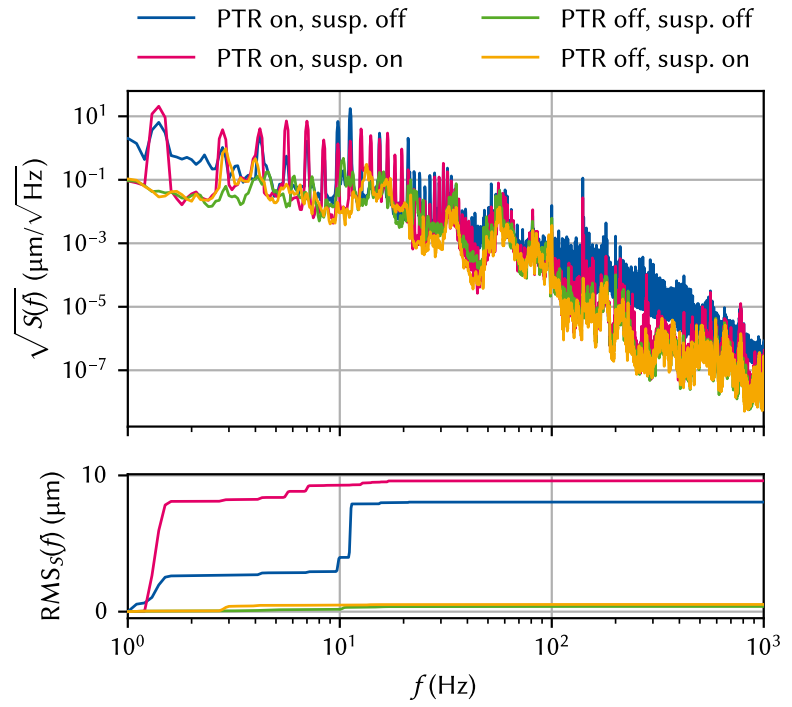


Figure 8.1

## 8.2 Optical vibration spectroscopy

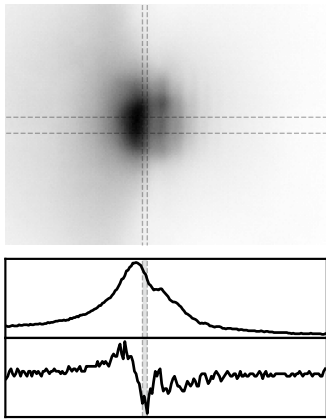


Figure 8.2

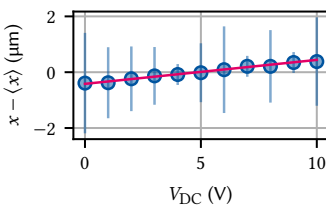
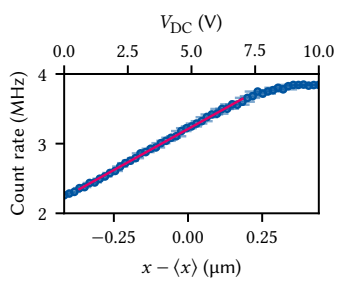


Figure 8.3



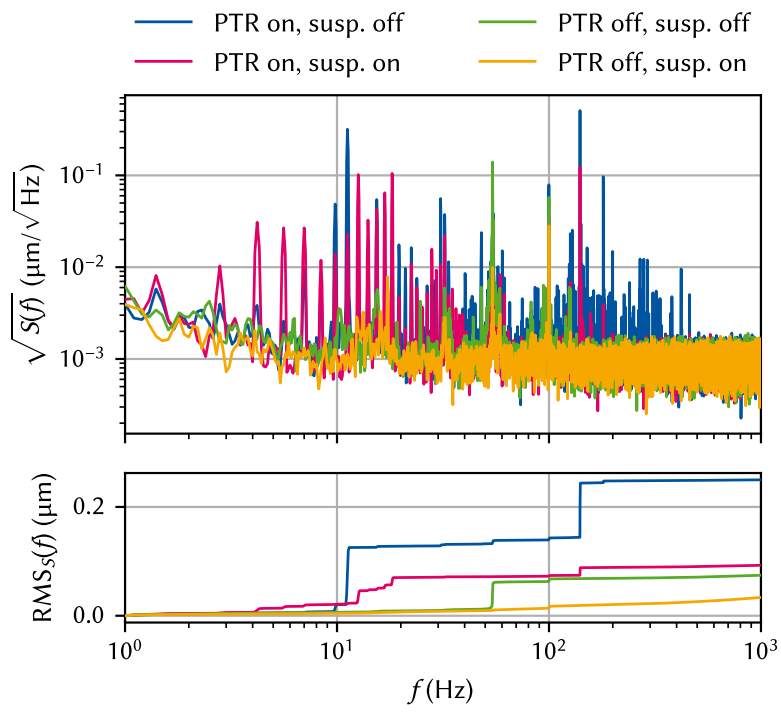


Figure 8.5





# Conclusion & outlook

9





**Part III**

**OPTICAL MEASUREMENTS OF  
ELECTROSTATIC EXCITON TRAPS IN  
SEMICONDUCTOR MEMBRANES**



## **Part IV**

# **A FILTER-FUNCTION FORMALISM FOR UNITAL QUANTUM OPERATIONS**



# **APPENDIX**





# Bibliography

- [1] Colin G. Gordon. “Generic Vibration Criteria for Vibration-Sensitive Equipment.” In: *Optomech. Eng. Vib. Control*. Optomechanical Engineering and Vibration Control. Vol. 3786. SPIE, Sept. 28, 1999, pp. 22–33. doi: [10.1117/12.363802](https://doi.org/10.1117/12.363802). (Visited on 10/14/2022) (cited on page 35).
- [2] Ray Radebaugh. “Cryocoolers: The State of the Art and Recent Developments.” In: *J. Phys.: Condens. Matter* 21.16 (Mar. 2009), p. 164219. doi: [10.1088/0953-8984/21/16/164219](https://doi.org/10.1088/0953-8984/21/16/164219). (Visited on 05/01/2025) (cited on page 35).
- [3] A. T. A. M. de Waele. “Basic Operation of Cryocoolers and Related Thermal Machines.” In: *J Low Temp Phys* 164.5 (Sept. 1, 2011), pp. 179–236. doi: [10.1007/s10909-011-0373-x](https://doi.org/10.1007/s10909-011-0373-x). (Visited on 05/01/2025) (cited on page 35).



# Special Terms

## D

**DR** dilution refrigerator. 35

## F

**FF** filter function. vii

## M

**MC** Monte Carlo. vii

## P

**PSD** power spectral density. v

**PT1** first pulse tube stage. 35

**PT2** second pulse tube stage. 35

**PTR** pulse tube refrigerator. 35

## Q

**QFT** quantum Fourier transform. viii

## S

**SRB** standard randomized benchmarking. viii

## T

**TEM** transmission electron microscope. 35